Article

Superior Cyclic Stability and Capacitive Performance of Cation- and Water Molecule-Preintercalated δ-MnO$_2$/h-WO$_3$ Nanostructures as Supercapacitor Electrodes

Md Shafayatul Islam, Sheikh Manjura Hoque, Mizanur Rahaman, Muhammad Rakibul Islam, Ahmad Irfan, and Ahmed Sharif*

Read Online

ACCESS | Metrics & More | Article Recommendations | Supporting Information

ABSTRACT: The large number of active sites in the layered structure of δ-MnO$_2$ with considerable interlayer spacing makes it an excellent candidate for ion storage. Unfortunately, the δ-MnO$_2$-based electrode has not yet attained the exceptional storage potential that it should demonstrate because of disappointing structural deterioration during periodic charging and discharging. Here, we represent that stable Na ion storage in δ-MnO$_2$ may be triggered by the preintercalation of K ions and water molecules. Furthermore, the sluggish reaction kinetics and poor electrical conductivity of preintercalated δ-MnO$_2$ layers are overcome by the incorporation of h-WO$_3$ in the preintercalated δ-MnO$_2$ to form novel composite electrodes. The composites contain mixed valence metals, which provide a great number of active sites along with improved redox activity, while maintaining a fast ion transfer efficiency to enhance the pseudocapacitance performance. Based on our research, the composite prepared from preintercalated δ-MnO$_2$ with 5 wt % h-WO$_3$ provides a specific capacitance of up to 363.8 F g^{-1} at a current density of 1.5 A g^{-1} and an improved energy density (32.3 W h kg^{-1}) along with an ~14% increase in capacity upon cycling up to 5000 cycles. Hence, the interaction between the preintercalated δ-MnO$_2$ and h-WO$_3$ nanorods results in satisfactory energy storage performance due to the defect-rich structure, high conductivity, superior stability, and lower charge transfer resistance. This research has the potential to pave the way for a new class of hybrid supercapacitors that could fill the energy gap between chemical batteries and ideal capacitors.
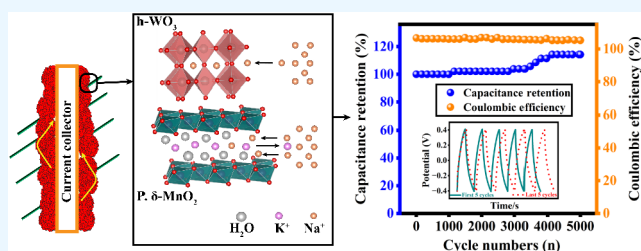
INTRODUCTION

The growing energy crisis and environmental degradation have sparked widespread interest in large-scale renewable energy storage systems. In order to address this need for renewable and transportable power sources, a lot of research effort has been put into developing high-performance energy storage devices over the last several decades.[1,2] Exploring innovative and cutting-edge electrode materials with electroactive sites for superior redox reactions with high electrical conductivity is crucial for improving energy storage.[3] Supercapacitors (SCs), batteries, and fuel cells are the most commonly used technologies in order to store and replenish energy. Among these candidates, the slow charging and draining rate is a major limitation for the batteries. Therefore, SCs containing aqueous electrolytes are being studied extensively as a potentially useful energy storage technology due to their high power density, great cycling stability, fast charge/discharge efficiency, long lifespan, environmental friendliness, and cost-efficiency, which can act as a gap-filler between conventional simple dielectric capacitors and batteries.[4,5] However, as long-lasting applications need a high energy density, the widespread use of SCs has been hampered by their relatively low energy density. The hybridization of SC with battery-type materials is the most

obvious way to achieve high energy density coupled to high power density inside a single device. Nevertheless, increasing the energy density without decreasing the power density via the rational design of innovative electrode materials remains a significant challenge.

Among the available alternatives to electrode materials for SCs, MnO$_2$ nanomaterials and vanadium-based materials stand out because of their superior theoretical capacity and easy fabrication.[6,7] Especially, MnO$_2$ possesses a lack of toxicity, a wide potential window, low cost due to its abundant availability, variable oxidation states, high surface area, and high theoretical capacitance, which contribute to its wide research in SC devices.[8] The synthesis route and reaction conditions determine the crystalline phases and morphologies of the MnO$_2$ nanostructures.[9] For instance, different methods,
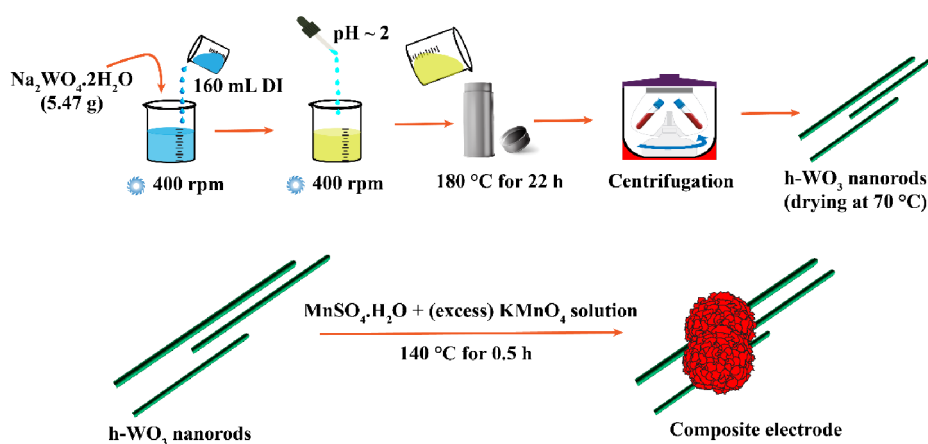
Figure 1. Schematic diagram of composites synthesis route.

such as the sol–gel technique,[10] coprecipitation,[11] and hydrothermal reaction,[12] have been used for the synthesis of nanostructured MnO$_2$ with various morphologies, such as hollow amorphous spheres, urchinlike structures, flowers, cubes, wires, belts, and tubes.[13−15] Electrodes prepared from varying crystalline structures of MnO$_2$ such as α, β, γ, and δ (depending on the face and edge sharing patterns of the repeating MnO$_6$ octahedron units) provide excellent electrochemical features for SC applications.[16] Among these crystalline phases, despite the fact that α-MnO$_2$ with 2 × 2 tunnels of 4.6 Å is a prominent focus in SC research owing to their better performance, δ-MnO$_2$ is theoretically much more appropriate for ion storage due to its layered structure with significantly bigger interspacing channels, about 7.0 Å.[9,17] Therefore, δ-MnO$_2$ might serve as a potential electrode material for adsorption as well as reversible insertion or extraction of electrolyte ions in aqueous SCs. Several studies have found that the specific capacitance values for δ-MnO$_2$ were between 80 and 110 F g^{-1}, which are relatively higher compared to other crystalline phases of MnO$_2$.[9,11]

The MnO$_2$ nanostructure functions well in neutral aqueous electrolytes and may store charge via nonfaradaic processes. But its widespread use in electrochemical applications is still constrained by poor ion mobility, poor rate capability, insufficient structural stability, and lower conductivity.[16,18] The low conductivity of MnO$_2$ (10^{-5}–10^{-6} S cm^{-1}) prevents it from displaying its full electrochemical capabilities when employed as an electrode material for SCs.[19] In addition, in a typical δ-MnO$_2$ system, the layered structure of δ-MnO$_2$ has a tendency to convert into various polymorphs. This alteration results in a drastic reduction in volume and a collapse of the underlying structure, which is the primary cause of the poor long-term cycle stability.[20] According to Munaiah et al., due to these intrinsic limits, the capacitance retention of δ-MnO$_2$ in Na$_2$SO$_4$ electrolyte was only 77% after tested for 50 cycles and 63% after 1000 cycles.[13] For δ-MnO$_2$, which has a flawless multilayer channel for Na$^+$ ion entrance, such an underwhelming performance is not desired. Furthermore, these features for energy storage devices lag significantly behind those of α-MnO$_2$.[21] The superior performance of the δ-MnO$_2$ electrode with its layered nature is highly expected.

The electrochemical performance of MnO$_2$-based electrodes has been enhanced by many methods to date, including nanostructuring, defect engineering, hybridization, and surface modification.[6] Among these, one of the best ways to improve

the specific capacitance of the δ-MnO$_2$ is to design the δ-MnO$_2$-based hybrid nanoarchitectures with other well-known pseudocapacitive transition metal oxides to meet the requirement of high-performance SCs utilizing the synergistic effect of each component.[6,22,23] For this, hexagonal tungsten oxide (h-WO$_3$) appears to be a promising candidate due to its high theoretical capacitance, higher conductivity (1.76 S cm^{-1}) compared to MnO$_2$, low cost, and environmental friendliness, which make it suitable for SC electrodes.[24,25] The short diffusion routes, varying oxidation states, and easy intercalation and deintercalation of electrolyte ions provide h-WO$_3$ with greater capacitance.[26]

In the present study, we preintercalated the δ-MnO$_2$ with water molecules and K$^+$ ions to stabilize the δ-MnO$_2$ polymorph framework as well as enhance the migration of electrolytic cations by activating the intrinsic high-performance of δ-MnO$_2$. The water molecules and K$^+$ ions serve as pillars by occupying the interstitial spaces created by the MnO$_6$ octahedron's arrangement.[27] K$^+$ was chosen as the intercalating cation because of its greater mobility and conductivity compared to common alkali cations like Li$^+$ and Na$^+$.[28] It was also observed that cation intercalation in the δ-MnO$_2$ framework aided in the ion diffusion process, thus emphasizing the significance of cation intercalation in δ-MnO$_2$.[29] Furthermore, binary composites of preintercalated flowerlike δ-MnO$_2$ and h-WO$_3$ nanorods were synthesized as electrode materials for SC devices via a simple sequential hydrothermal treatment, and the effect of the concentrations of h-WO$_3$ nanorods on the capacitive performance of the composite electrode has been analyzed for the first time. Mesoporous flowerlike δ-MnO$_2$ exhibits a short diffusion path and more channels for ions of the electrolyte.[30] As a result, the energy storage capability may be boosted by using flower-shaped nanostructured electrodes. Additionally, the insertion of h-WO$_3$ results in a defect-rich surface of the electrode, which may result in more active sites for the intercalation of ions.[31] The major purpose of using the nanorod morphology of h-WO$_3$ is to strengthen the long-distance connection between the nanosheets of porous δ-MnO$_2$ flowers, providing a channel to diffuse the ions from the electrolyte into the inner cores of δ-MnO$_2$ flowers. When used as a host for Na$_2$SO$_4$ electrolytes, these composites exhibit superior cyclic stability and an impressive performance in Na ion storage, overcoming the limitations in earlier studies on δ-MnO$_2$. Hence, as a result of adjusting the material architecture, the electrochemical

performance of the synthesized binary hybrid was enhanced, making it amenable to the fabrication of the desired energy storage devices.

■ MATERIALS AND METHODS

Materials. All the chemical reagents (obtained from Merck, Germany) such as manganese sulfate monohydrate ($MnSO_4 \cdot H_2O$), potassium permanganate ($KMnO_4$), sodium tungstate dehydrate ($Na_2WO_4 \cdot 2H_2O$), poly(vinyl alcohol) (PVA), dimethyl sulfoxide (C_2H_6OS), sodium sulfate (Na_2SO_4), ethanol, and hydrochloric acid (HCl) used in this research were of analytical grade and put to use without any further purification. Deionized (DI) water of the highest purity (with a resistivity of 18.2 MΩ·cm) was utilized throughout the experiment.

Sample Preparation. The samples were synthesized by following the hydrothermal route. The schematic diagram of the synthesis route is presented in Figure 1.

Synthesis of K Ion- and Water Molecule-Preintercalated δ-MnO$_2$-Layered Nanostructures. The desired layered nanostructures were prepared by using a facile hydrothermal approach. Initially, $MnSO_4 \cdot H_2O$ (9.5 mmol, 2.13 g) and an excess amount of $KMnO_4$ (33.5 mmol, 5.3 g; as a source of K) were dissolved in 160 mL of deionized water to prepare a precursor solution. After magnetically stirring the resulting mixture for 1 h, a uniform pink solution was obtained. Afterward, the solution was transferred to a 250 mL Teflon-lined stainless-steel autoclave. The autoclave was heated at 140 °C for 0.5 h before being cooled to room temperature. To remove any trace of the solvents, the resulting black powder was washed three times with ethanol (15 mL) and three times with water (15 mL) by centrifugation and subsequent removal of the supernatant. Finally, the preintercalated δ-MnO$_2$ product was obtained by drying the product at 70 °C overnight in a vacuum and denoted as P.δ-MnO$_2$. Hence, flowerlike P.δ-MnO$_2$ nanosheets were easily synthesized using a fast and cost-effective synthesis route.

Synthesis of h-WO$_3$ Nanorods. In a typical process, $Na_2WO_4 \cdot 2H_2O$ (5.47 g) was added to 160 mL of distilled water under vigorous magnetic stirring to prepare a homogeneous solution. During stirring, a 3 M HCl aqueous solution was added dropwise to set a pH value of ~2.0. After stirring for 2 h, the greenish-yellow solution was moved to a 250 mL Teflon-lined stainless-steel autoclave and heated for 20 h in an electric oven at 200 °C operating temperatures. After being cooled to ambient temperature, the precipitates were washed and dried to obtain the desired h-WO$_3$ nanorods.

Synthesis of Preintercalated δ-MnO$_2$/h-WO$_3$ Composites. To incorporate h-WO$_3$ into the preintercalated δ-MnO$_2$-layered structure, an appropriate amount of h-WO$_3$ nanorods were introduced to 60 mL of distilled water and then sonicated for 1 h using a probe sonicator. Then a 110 mL solution of $MnSO_4 \cdot H_2O$ and excess $KMnO_4$ were sonicated and vigorously agitated in the 60 mL h-WO$_3$ solution for several hours. The mixture was then placed in a Teflon-lined autoclave and heated at 140 °C for 0.5 h in an oven. After washing and drying at 70 °C for several hours, the desired composite was finally obtained. In this work, different weight percentages (3, 5, and 7 wt %) of h-WO$_3$ nanorods were incorporated into the preintercalated δ-MnO$_2$ (P.δ-MnO$_2$) matrix to make the composite electrodes. The 3, 5, and 7 wt % h-WO$_3$-incorporated composites are denoted as P.δ-MnO$_2$/W-a, P.δ-MnO$_2$/W-b, and P.δ-MnO$_2$/W-c, respectively.

Materials' Characterization. For structural studies, the diffraction peaks were characterized using an X-ray diffractometer [Rigaku] at room temperature (Cu X-ray radiation of wavelength K_{α_1} = 1.5406 Å and a scanning rate of 5°/min). X-ray photoelectron spectroscopy (XPS) was used to investigate the presence of various oxidation states of the elements on the surface of samples via a Thermo Fisher Scientific instrument (Escalab Xi+) equipped with monochromatic Al K_α radiation. At a heating rate of 10 °C/min, a PerkinElmer Pyris Diamond TG/DTA analyzer was used to conduct a thermogravimetric analysis (TGA) from room temperature up to 500 °C in air. In addition, the samples were analyzed by Fourier transform infrared (FTIR) spectroscopy (Shimadzu, IRSpirit-T, Japan) to determine their molecular composition. The surface morphology and structural analyses of the samples were performed using the field emission scanning electron microscope (FESEM: JEOL, JSM, 7600F) and transmission electron microscope (TEM: Talos F200X, Thermo Fisher Scientific, USA). By utilizing Gatan and ImageJ software, the images from the SEM and TEM were analyzed.

Electrochemical Characterizations. *Electrodes' Preparation.* A homogeneous slurry comprising the synthesized samples as an electrode material, dimethyl sulfoxide as a solvent, and PVA as a binder was uniformly cast onto a graphite rod surface, maintaining a mass loading of ~0.5−1 mg cm^{-2}. The electrode material mass (m) was determined by comparing the electrode's pre- and postdeposition weights. PVA (4 wt % of electrode material) and dimethyl sulfoxide were mixed with the synthesized samples to prepare the desired slurry of electrode materials. PVA's multiple hydroxyl groups may form strong hydrogen bonds with both the active materials and the current collector, making it an ideal binder for high-capacity electrodes.[32] After being sonicated for 1 h, each of these mixes was deposited onto a glassy carbon electrode. The electrodes were then dried at 60 °C for several hours to be used as working electrodes.

Electrochemical Measurements. The electrochemical performance of the as-prepared materials was evaluated by using a CS310 electrochemical workstation (Corrtest, China) and conventional three-electrode systems. The synthesized sample was placed on a glassy carbon electrode as the working electrode, an Ag/AgCl (saturated KCl) electrode as the reference electrode, and a platinum plate as the counter electrode. The electrochemical performance was studied via cyclic voltammetry (CV), galvanostatic charge−discharge (GCD) measurements, and electrochemical impedance spectroscopy (EIS) in a 0.5 M Na_2SO_4 aqueous solution. The measurements were carried out with a working potential window of −0.4 to 0.4 V, and the EIS measurements were carried out using a sinusoidal signal over a frequency range from 0.1 to 10^5 Hz. From the GCD results, using the following equations, the specific capacitance (C_{sp}), power density (P), and energy density (E) of the system were calculated:[8]

$$C_{sp} \ (\text{F g}^{-1}) = \frac{I \Delta t}{m \Delta V} \tag{1}$$

$$E \ (\text{W h kg}^{-1}) = \frac{C_{sp} \Delta V^2}{2 \times 3.6} \tag{2}$$

$$P \ (\text{W kg}^{-1}) = \frac{E \times 3600}{\Delta t} \tag{3}$$
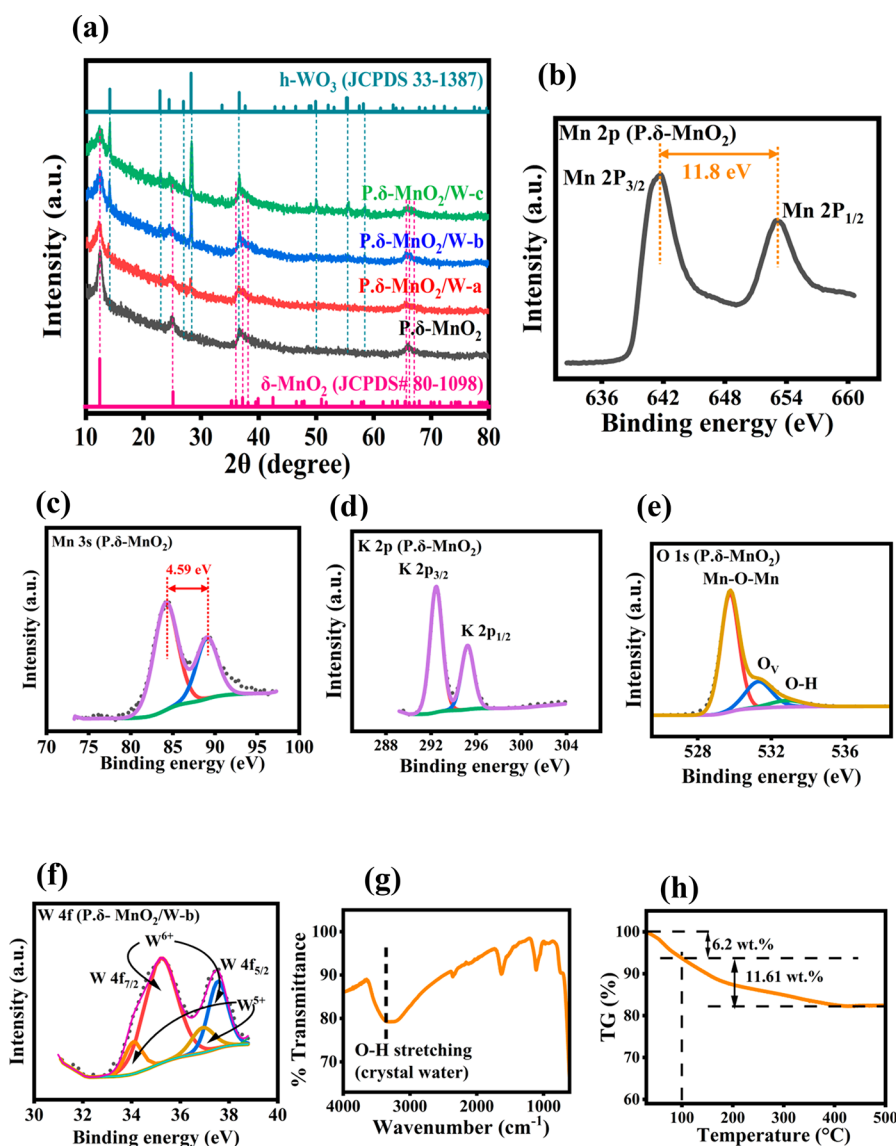
Figure 2. (a) XRD pattern of P.δ-MnO$_2$ and the composites, (b−e) high-resolution XPS spectra of Mn 2p, Mn 3s, K 2p, and O 1s, respectively, from P.δ-MnO$_2$, (f) high-resolution XPS spectra of W 4f from P.δ-MnO$_2$/W-b composites, (g) FTIR analysis of P.δ-MnO$_2$, and (h) TGA curve of P.δ-MnO$_2$ sample from room temperature to 500 °C.

Where I = applied current on the electrode material, Δt = discharge time, m = active mass, and ΔV = working potential window. The capacitance retention and columbic efficiency were calculated by using equations:[33,34]

$$\text{Capacitance retention } (\%) = \frac{n\text{th cycle capacitance}}{1\text{st cycle capacitance}} \times 100 \tag{4}$$

$$\text{Coulombic efficiency, } \eta = \frac{t_{\text{discharge}}}{t_{\text{charge}}} \times 100 \tag{5}$$

All of the provided electrochemical data were obtained after the electrodes had been stabilized.

RESULTS AND DISCUSSION

The room-temperature powder X-ray diffraction (XRD) spectra of the samples are depicted in Figure 2a. These spectra were studied to identify different phases, crystallographic structures, and the purity of the samples. It is noted that the diffractogram of P.δ-MnO$_2$ represents four peaks centered at 12.44°, 24.97°, 36.77°, and 65.77°. These signature peaks are consistent with a layered P.δ-MnO$_2$ structure following JCPDS no. 80-1098 ($C2/m$ space group), which is a birnessite framework in the base-centered monoclinic phase.[35,36] Notably, no impurity peaks were identified in the XRD spectra, which proves the high purity of the δ-MnO$_2$ nanostructure. According to the JCPDS card, these peaks may be ascribed to the (001), (002), (−111), and (020) planes. The extremely tiny crystallites in powdered specimens cause diffraction lines to have a noteworthy width due to their entirely random orientations, and the diffraction lines are likely to merge, resulting in broad peaks.[37] Multiple lines in the (−111) and (020) peak regions might have been affected by this, which led to broad 36.77° and 65.77° peaks in the diffractogram. The signal-to-noise ratio of the diffractogram is also very high. These weak and diffuse XRD peaks reveal the poor polycrystalline nature of the synthesized P.δ-MnO$_2$ nanostructure. The most intense peak (001) reveals a well-stacked interlayer distance along the c-axis, similar to what has

been documented for other birnessites.[38] The periodicity along the c-axis is also reflected by the (002) plane.

The detailed surface oxidation state and chemical composition of the P.δ-MnO$_2$ nanostructure were studied by X-ray photoelectron spectroscopy (XPS). In the XPS survey spectrum of P.δ-MnO$_2$, displayed in Figure S1, the Mn 2p peak is clearly apparent in the 635−660 eV range. Moreover, the survey spectrum of the δ-MnO$_2$ nanostructure contains peaks of K 2p, C 1s, and O 1s, demonstrating the presence of their respective atoms. Surface contamination accounts for the occurrence of the C 1s peak in the survey spectrum. The high-resolution narrow scan spectra of Mn 2p, Mn 3s, K 2p, and O 1s are displayed in Figure 2b−e. The Shirley background subtraction of the spectrum is used for all atoms. As depicted in Figure 2b, P.δ-MnO$_2$ consisted of a doublet of Mn 2p$_{3/2}$ at 641.8 eV and Mn 2p$_{1/2}$ at 653.6 eV with an energy difference of 11.8 eV, which is consistent with the standard spectrum of MnO$_2$.[39] In addition, the synthesis of Mn^{4+} is further confirmed by the lack of a satellite peak between Mn 2p$_{3/2}$ and Mn 2p$_{1/2}$. Spin orbit coupling accounted for the energy difference between the 2p$_{3/2}$ and 2p$_{1/2}$ peaks. Two Mn 3s peaks have a splitting energy of 4.59 eV (Figure 2c). Therefore, the average oxidation state of Mn in the synthesized P.δ-MnO$_2$ sample is determined by using the following equation:[39]

$$AOS = 8.95 - 1.13\Delta E \text{ (eV)} \tag{6}$$

Where ΔE denotes the energy difference between the primary Mn 3s peak and its satellite peak. Hence, based on the splitting energy of the Mn 3s peak, the average oxidation state of the resultant P.δ-MnO$_2$ sample was calculated to be 3.76. A peak at 292.45 eV of K 2p$_{3/2}$ (Figure 2d) indicates the existence of K, and the calculated K/Mn ratio is 0.23. Because of the presence of K$^+$ ions, Mn's oxidation state is predicted to be about 3.77, which is in line with the estimated value from the XPS analysis. As depicted in Figure 2e, the deconvoluted asymmetric O 1s spectrum can be fitted using three Gaussian components corresponding to three peaks at 529.74 eV (lattice oxygen, Mn−O−Mn bond), 531.29 eV (oxygen-deficient regions, O$_V$), and 532.85 eV (adsorbed surface water, O−H bond).[8,40] The as-prepared product is thus found to have the chemical formula K$_{0.46}$Mn$_2$O$_4$.

Subsequently, the FTIR technique was also used to confirm the presence of structural water. In the FTIR spectrum, illustrated in Figure 2g, a broad absorption band in the range of 3000−3600 cm^{-1} may be credited to the stretching vibration of the hydroxyl group (interlayer water), which is further confirmed by 1630 and 1110 cm^{-1} band positions that are usually due to the O−H bending vibrations combined with Mn atoms.[41] The bands at about 721 cm^{-1} can be attributed to the Mn−O vibrations of the MnO$_6$ octahedron.[3] Combined with FTIR, the interlayer water content was analyzed using thermogravimetric analysis (TGA) in a N$_2$ atmosphere. The thermogram (Figure 2h) demonstrated that at temperatures as high as 100 °C, ~6.2 wt % water was lost as a result of physical evaporation from the surface. From 100 to 450 °C, an additional 11.61% of weight loss occurs owing to the elimination of interlayer water, verifying the existence of structural water. Thus, the conformation of bound water confirms the close resemblance of the molecular formula of the P.δ-MnO$_2$ structure with the standard K$_{0.46}$Mn$_2$O$_4$·1.4H$_2$O layered structure (JCPDS no. 80-1098). These layers are built using a Mn−O sheet, which consists of edge-shared MnO$_6$ octahedra in a coplanar arrangement that can accommodate

both water molecules and exchangeable cations in the interlayer gap to serve as the stabilizing agent. This crystal water acts as pillars to stabilize the interlayer and framework of δ-MnO$_2$. The presence of these cations and water molecules between P.δ-MnO$_2$ layers further inhibits the transition from MnO$_2$ to Mn$_2$O$_3$ and encourages the intercalation of electrolyte ions due to the high water content.[42]

Moreover, the diffraction peaks in the composites contain planes of hexagonal WO$_3$ phase along with the P.δ-MnO$_2$ phase. All the sharp diffraction peaks are well indexed to the hexagonal structure of h-WO$_3$ (JCPDS no. 33-1387) (Figure S2).[43] It is noticed (from Figure 2a) that as the amount of the filler h-WO$_3$ increases in the composite composition, the peaks belonging to h-WO$_3$ become more intense, which is due to the difference in the crystallinity of P.δ-MnO$_2$ and h-WO$_3$. Furthermore, the XPS survey spectrum of P.δ-MnO$_2$/W-b, displayed in Figure S1, confirms the presence of a W 4f core level peak in the 32−38 eV range. Figure 2f shows that the high-resolution W 4f core level spectrum may be deconvoluted into four peaks, corresponding to W 4f$_{5/2}$ and W 4f$_{7/2}$ levels. Binding energy peaks at 35.3 and 37.5 eV are associated with the W^{6+} state, whereas those at 34.1 and 37 eV are associated with the W^{5+} state, which indicates the existence of mixed oxidation states of the h-WO$_3$ phase in the composite.[44] W^{6+} is more intense than W^{5+}, suggesting that h-WO$_3$ is mostly in the W^{6+} form.

The Scherrer formula was used to calculate the sizes of the crystallites. The equation of Scherrer's formula[45] can be written as

$$D = \frac{k\lambda}{\beta \cos \theta} \tag{7}$$

where D is the crystallite size, β is the full width half-maximum of the diffraction peak, and k is equal to 0.9. Using the dislocation density parameter (δ), the number of dislocations in a crystal might be determined using the equation:[45]

$$\delta = \frac{1}{D^2} \tag{8}$$

Furthermore, microstrain was determined using the following equation:[46]

$$\varepsilon = \frac{\beta}{4 \tan \theta} \tag{9}$$

where ε is the microstrain.

The calculated crystallite size, microstrain, and dislocation density values corresponding to the (001) characteristic peak of the P.δ-MnO$_2$ and composites samples are tabulated in Table 1.

Figure 3 shows the variation of the crystallite size, d spacing, microstrain, and dislocation density with the concentration of

Table 1. Calculated Crystallite Size, Microstrain, and Dislocation Density of δ-MnO$_2$ and the Composite Samples

samples	crystallite size (Scherrer's formula), D (nm)	microstrain, $\varepsilon \times 10^{-3}$	dislocation density, $\delta \times 10^{-3}$ (nm^{-2})
P.δ-MnO$_2$	7.36	45.38	18.45
P.δ-MnO$_2$/W-a	6.25	53.93	25.64
P.δ-MnO$_2$/W-b	5.47	61.72	33.36
P.δ-MnO$_2$/W-c	5.73	57.91	30.42
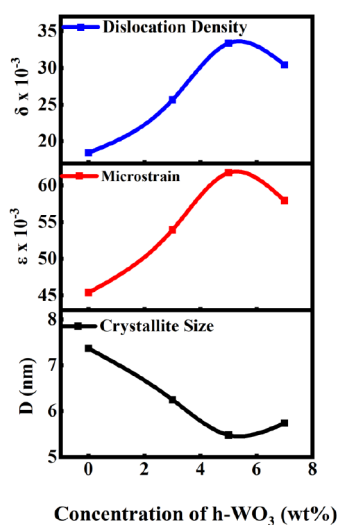
Figure 3. Variation of crystallite size, microstrain, and dislocation density as a function of increasing concentration of h-WO$_3$.

Figure 4. (a,b) Representative FE-SEM images of P.δ-MnO$_2$ flowers and h-WO$_3$ nanorods, respectively; (c−e) FE-SEM images of P.δ-MnO$_2$/W-a, P.δ-MnO$_2$/W-b, and P.δ-MnO$_2$/W-c composites, respectively; (f,h) TEM images and (g,i) corresponding SAED patterns of P.δ-MnO$_2$ flowers and h-WO$_3$ nanorods, respectively.

h-WO$_3$ in P.δ-MnO$_2$. The broadening and decreasing intensity of the (001) planes for the composites compared to P.δ-MnO$_2$ imply an increase in the amorphous characteristics. The interlayer spacing may be altered alongside the deteriorating crystallite size, which may enhance the number of reactive sites and the intercalation/deintercalation kinetics of charge carriers between active materials and electrolyte solutions during the charging/discharging process.[47] Increased microstrain might generate defects like dislocations, imperfect crystal structures, and vacancies, which help with fast ion diffusion on the electrode surface.[48]

Furthermore, to confirm the orientation and morphology of P.δ-MnO$_2$ and the composites, field emission scanning electron microscopy (FE-SEM), transmission electron microscopy (TEM), and high-resolution transmission electron microscopy (HR-TEM) analyses were synergistically employed. Figure 4a shows the image of a three-dimensional marigold flower-type structure with a diameter of 400−600 nm constructed by intersecting curved multilayer nanosheets (as petals construct a flower). These nanosheets possess clean and smooth surfaces and have thicknesses of ∼9−16 nm. The reaction involved in the synthesis of P.δ-MnO$_2$ flowers is:

$$3MnSO_4 + 2KMnO_4 \text{ (excess)} + 2H_2O$$
$$\xrightarrow[\text{30minutes}]{140\ °C} 5P.\delta\text{-}MnO_2 \text{ (flowers)} + 2H_2SO_4 + K_2SO_4$$
$$(10)$$
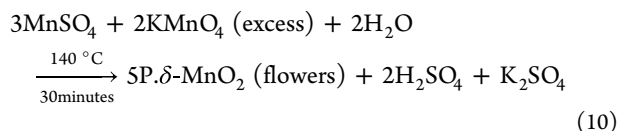
Due to the fact that the flowerlike P.δ-MnO$_2$ nanosheets self-assemble in a nonparallel random fashion, an interconnected porous morphology with ultrathin nanosheets is formed. This specific 3D porous structure with macropores allows rapid diffusion of the electrolytes from the macropores to the micropores throughout the nanosheet network. It is anticipated that a large specific surface area with increased electron tunnel regions would result from such a configuration. This is suitable for application in pseudocapacitors, as electrochemical reactions rely on active spots on the surface of the substance for better redox capacity and mass transfer rate.[49] This effective electrochemical process on the P.δ-MnO$_2$ nanostructure ultimately improves the material's capacitive properties. The porous structure facilitates full access of the
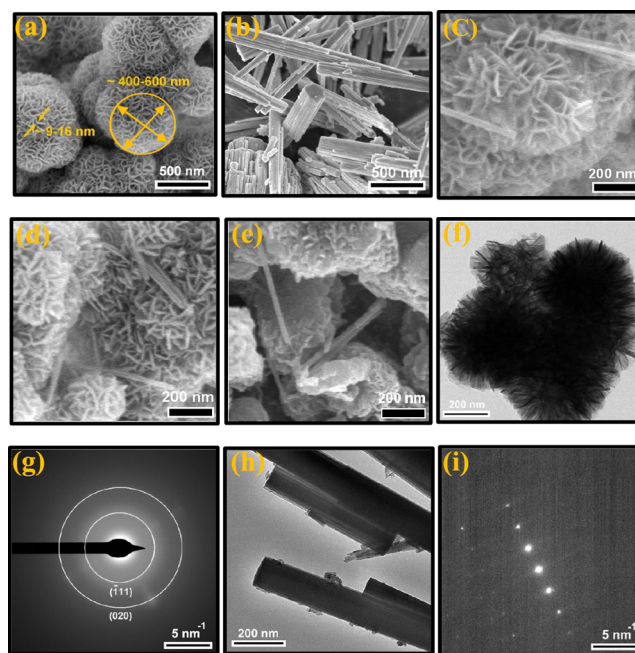
electrolyte to the electrode materials and maximizes the utilization of P.δ-MnO$_2$. That is to say, Na$^+$ ions are intercalated or extracted not only at the surface but also inside the pores.[31,50] Hence, Na$^+$ ion transport is aided by the P.δ-MnO$_2$'s distinctive morphology, which includes structural flaws and readily accessible metal centers, leading to improved electrode−electrolyte interaction.

On the other hand, the h-WO$_3$ nanorods were obtained through a facile hydrothermal treatment as follows:

$$Na_2WO_4\cdot 2H_2O + 2HCl + nH_2O$$
$$\xrightarrow[\text{pH}=2]{200\ °C\ (20\text{hours})} h\text{-}WO_3 \text{ (nanorods)} + 2NaCl$$
$$+ (n+1)H_2O \qquad (11)$$
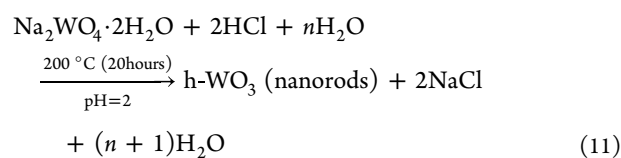
The FE-SEM image (Figure 4b) of the sample at pH = 2 shows irregular nanorods with lengths in the range 0.2−2 μm and a diameter of ∼20−50 nm. However, a few nanorods displayed broken edges as a consequence of incomplete growth during synthesis. Surface morphology made of these nanorods improves the electrochemical performance of composites by increasing surface area, electroactive sites, and metalactive centers during electrochemical processes.[51] As an added bonus, the existence of these nanorods creates countless new transport channels or paths for the ion's movement and accumulation.[51]

Figure 4 represent the FE-SEM images of the composite materials. In all three cases, the original microflowers' nanosheets are tangled up with the nanorods. One end of each nanorod is embedded in the nanosheets, suggesting the growth of a sparking flower via the formation of a P.δ-MnO$_2$ nucleus on the surface of h-WO$_3$ nanorods because of van der Waals, cohesive, electrostatic, or other chemical forces.[52] Thus, h-WO$_3$ might act as a backbone for the host P.δ-MnO$_2$. Effective transfer of electrolyte ions inside a large porous P.δ-

MnO$_2$ flower is facilitated due to close integration between P.δ-MnO$_2$ (3D flower) and h-WO$_3$ (1D nanorod), which may also provide structural stability that can help to achieve excellent rate performance along with superior cycling stability. The h-WO$_3$ nanorods provide an easy path for the transportation of electrolyte ions, decreasing the internal resistance.[15] However, with the increase in the concentration of h-WO$_3$, aggregation between the nanosheets of P.δ-MnO$_2$ is observed (Figure 4e). The flowerlike surfaces tend to collapse and become largely agglomerated, which may be due to the unstable nature of P.δ-MnO$_2$ nanosheet layers.[34] Additionally, compared to the original microflowers, the P.δ-MnO$_2$ nanosheets' edges have become rougher (Figure 4a versus e).

Additionally, TEM and HR-TEM investigations reveal the atomic-level crystalline details of the nanostructures. Selective area electron diffraction (SAED) patterns and TEM images of P.δ-MnO$_2$ nanostructures and h-WO$_3$ nanorods are shown in Figure 4f−i. The TEM image of P.δ-MnO$_2$ (Figure 4f) shows the assembly of nanosheets similar to the SEM image in Figure 4a, with an ultrathin thickness that is consistent with the partially transparent nanosheets at the edge of the flowers. Weak diffraction rings in the SAED pattern confirm the poor crystallinity of the P.δ-MnO$_2$ nanostructure (Figure 4g). Diffraction rings originating from the (−111) and (020) reflections of P·δ-MnO$_2$ are observed in the SAED pattern. Due to the probability of the nanosheet surfaces being parallel to the electron beam, the diffraction rings of (001) and (002) planes of P.δ-MnO$_2$ in the SAED pattern cannot be identified. Figure 4h displays the nanorod bundle morphology, which is composed of many highly ordered nanorods. The SAED pattern (Figure 4i) reveals well-defined diffraction spots, confirming the single-crystalline structure of the h-WO$_3$ nanorods. The SAED pattern could be indexed to the [010] zone axis of h-WO$_3$, which also confirms the hexagonal packing of WO$_3$ nanorods.[53]

HR-TEM images of the samples show the folded nature of the P.δ-MnO$_2$ nanosheets (insets of Figure 5). The observed discontinuity in the lattice fringes of the curled edges suggests the presence of excess dislocations and defects in the crystals.[54] The HR-TEM images confirm the polycrystalline nature of the P.δ-MnO$_2$ samples, as each nanosheet consists of numerous tiny domains with various orientations. The HR-TEM image of the edge of P.δ-MnO$_2$ nanosheets in the inset of Figure 5a shows the lattice spacing of the (001) plane (highlighted by the lines) to be 0.71 nm, which further demonstrates the intercalation of crystal water into the layers of the birnessite-MnO$_2$ (i.e., δ-MnO$_2$).[55] Furthermore, the lattice spacing corresponding to the (001) planes of P.δ-MnO$_2$ is found to be 0.716, 0.721, and 0.706 nm for P.δ-MnO$_2$/W-a, P.δ-MnO$_2$/W-b, and P.δ-MnO$_2$/W-c samples, respectively (Figure 5b−d). The gradual increase in interlayer spacing of the composite with the increase in the h-WO$_3$ concentration may be due to the diffusion of W^{6+} ions between layers of P.δ-MnO$_2$. This widening of lattice fringes may be traced back to the introduction of flaws in the crystal structure.[56] This shortens the path of the electrolyte ion by providing storage sites that are accessible to the electrolyte ions. However, a reduction in the lattice spacing of P.δ-MnO$_2$/W-c may be attributed to the potential lattice rearrangement. The slight shift of the (001) peak compared to pristine δ-MnO$_2$ owing to the incorporation of higher wt % of h-WO$_3$ is evident from XRD analysis (a right shift of the (001) peak compared to pristine δ-MnO$_2$ was observed). This lattice distortion might have also resulted in
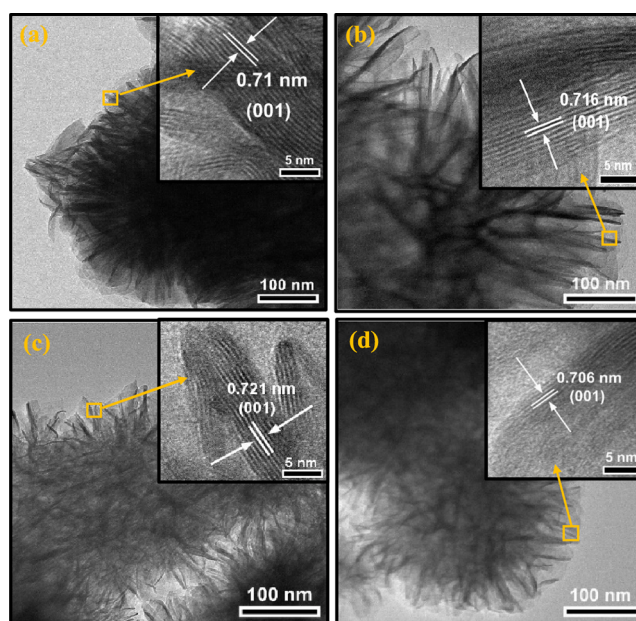
Figure 5. Regular TEM images of the (a) P.δ-MnO$_2$, (b) P.δ-MnO$_2$/W-a, (c) P.δ-MnO$_2$/W-b, and (d) P.δ-MnO$_2$/W-c flowers' nanosheets. Insets of (a−d) show the corresponding HR-TEM images.

the deintercalation of some of the water molecules from the interlayer spacing.[55]

The enlargement of interlayer spacing, ultrathin thickness of nanosheets, and unique flower-rod morphology provide better ion intercalation, more electroactive sites, and fast electron transportation that give desired electrochemical properties with improved efficiency in attaining higher capacitance.[57] While interlayer spacing is used for charge agglomeration and charge storage, the macropores could act as channels for rapid ion transport.

To evaluate the electrochemical performance of these nanostructures as active supercapacitor electrodes, we performed CV, GCD, and EIS measurements. The charge transfer rate between the electrolyte and electrode was analyzed by using cyclic voltammetry (CV). An ideal rectangular shape and symmetric current response of the CV curves indicate the pure electrical double layer capacitance (EDLC) charge storage mechanism, while the existence of the faradic pseudocapacitive charge storage mechanism is indicated by the departure from the rectangular form.[58] Both mechanisms are proposed for charge storage in the P.δ-MnO$_2$ nanostructure, considering the quasi-rectangular shape of the CV curve at 60 mV/s in Figure 6a. As a result, the CV curve is indicative of a mixture of EDLC and pseudocapacitive behavior. In the first mechanism, alkali cations adsorb or desorb onto the electrode/electrolyte interface, respectively, via a surface process, such as

$$(\text{P.}\delta\text{-MnO}_2)_{\text{surface}} + \text{Na}^+ + \text{e}^- \leftrightarrow (\text{P.}\delta\text{-MnO}_2\cdot\text{Na})_{\text{surface}}$$

$$(12)$$
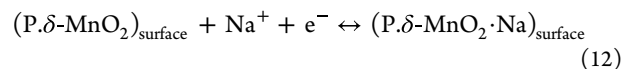
The second mechanism is the intercalation or extraction of alkali cations (Na$^+$) from the electrolyte into the bulk of the P.δ-MnO$_2$ nanostructure along with preintercalated K$^+$, as transition metal oxides like δ-MnO$_2$ have unoccupied orbitals that may intercalate with Na$^+$ ions.[28,59−61] The layered
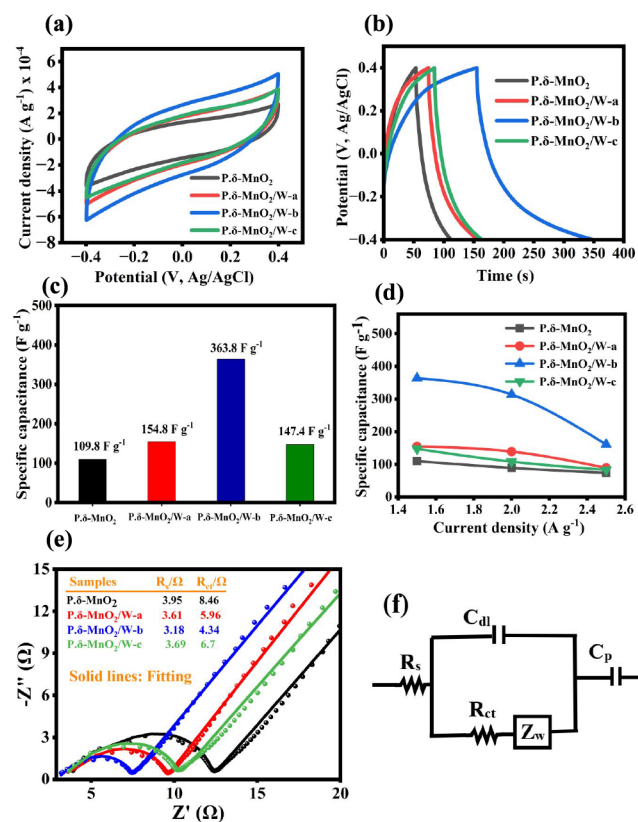
Figure 6. Electrochemical measurements of the P.δ-MnO$_2$, P.δ-MnO$_2$/W-a, P.δ-MnO$_2$/W-b, and P.δ-MnO$_2$/W-c samples in the three-electrode system for SC studies: (a) CV curves at a fixed scan rate of 60 mV/s, (b) GCD curves at a fixed current density of 1.5 A g^{-1}, (c) comparison of specific capacitances for each sample, (d) variation of specific capacitance with increasing current densities, (e) Nyquist curves for experimental and fitted data, and (f) equivalent circuit of Randle's model.

structure of P.δ-MnO$_2$ allows for the transportation of Na$^+$ ions between the layers:

$$\text{P.}\delta\text{-MnO}_2 + \text{Na}^+ + \text{e}^- \leftrightarrow (\text{P.}\delta\text{-MnOONa})_{\text{intercalation}};$$

$$(\rightarrow \text{during discharging}) \tag{13}$$
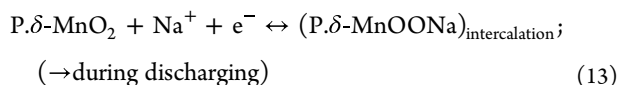
For amorphous samples like ours, the surface process is more prominent, as indicated by the CV curve, which involves the adsorption and desorption of Na$^+$ ions from the electrolyte into the surface of nanostructured P.δ-MnO$_2$.

Furthermore, from the CV curves of the composites (Figure 6a), more deviation from the ideal rectangular shape appears. Hence, for composites, the diffusion-controlled process is becoming the defining mechanism for charge storage. This is due to the additional intercalation or extraction of Na$^+$ ions by h-WO$_3$ to store energy as a transition between oxidation states of W might lead to Faradaic electron transfer. It suggests that the oxidation level of W is reduced to the W^{5+} state and then is oxidized back to the W^{6+} state during Na$^+$ ion intercalation and extraction, respectively, via a reversible redox reaction between W^{6+} and W^{5+} ions at the surface (the presence of both oxidation sates in the composite sample was confirmed by the XPS analysis, Figure 2f). The reaction mechanism is shown below:

$$\text{h-WO}_3 + \text{Na}^+ + \text{e}^- \leftrightarrow (\text{h-WO}_3\text{Na})_{\text{intercalation}} \tag{14}$$

Moreover, incorporation of h-WO$_3$ nanorods into the composites adds more redox-active sites for the insertion of Na$^+$ ions and contributes to a greater current density, as metallic W might serve as a current reservoir for h-WO$_3$, which increases conductivity in binary composites.[62,63] Because of this, a relatively larger integral area is noticed in Figure 6a for the composites when compared to the P.δ-MnO$_2$ electrode. Thus, a higher capacitive performance is achieved by the superior utilization of the electrode material. Besides, the presence of h-WO$_3$ in the composites creates a fast route, enhancing current responsiveness and minimizing internal resistance to boost charge carrier mobility. As the P.δ-MnO$_2$ flowers were larger, the alkaline Na$^+$ ions had a harder time penetrating the material and reaching the inner surface. In our experiment, the as-prepared h-WO$_3$ nanorods facilitate the transport of solvated Na$^+$ to the interior of P.δ-MnO$_2$ flowers, leading to a high pseudocapacitance.

However, Figure 6a also depicts that the area of the CV curve decreases at a higher concentration of h-WO$_3$ nanorods (P.δ-MnO$_2$/W-c sample) in the composites, which can be tracked back to the collapse of the porous structure by the agglomeration of nanosheets. This phenomenon reduces the interlayer spacing, which in turn limits the ion diffusion and decreases the chance of storage due to restricted redox reactions. Furthermore, P.δ-MnO$_2$ and composites were analyzed at different scan rates of 20, 40, 60, and 80 mV/s, as shown in Figure S3. The CV curves had a leaflike shape at all scan rates with no clear redox peaks, which indicates that the electrode materials have good electrical double-layer capacitance and a larger surface area with a lot of electroactive sites for ion transfer.[64] The lack of redox peaks in the CV curves suggests the existence of constant-rate reversible electrochemical reactions in the materials.[65] Moreover, ultra-fast charge-transfer kinetics, reversible redox processes, and simple access to electrolyte ions at the interface between electrode and electrolyte are all inferred from the almost repeatable and conserved form of CV curves, even at high scan rates.[8] At a low scan rate, the output current is minimal because the ions have more time to disperse in the active material's microscopic pores, promoting greater charge storage. At a higher scan rate, the probability of storage is reduced because ion diffusion limits the pace of redox reactions[16] and increases the output current due to the formation of a thinner diffusion layer, which allows more electrolytic ions to make contact with the electrode material. In addition, the CV curves are very symmetrical at different scan rates. The CV curves show near-mirror image current acknowledgment when the voltage changes. This means that the prepared electrode materials are less resistant to charge transfer and ion diffusion. For higher sweep rates, the CV loop area also grows due to the increased current response through the circuit.[3] Moreover, Figure S6 shows the decoupling of the capacitive contribution of the samples. It is noticed in Figure S6 that the EDLC contribution dominates for the P.δ-MnO$_2$ sample. It is indicated that 77% of the total capacity is contributed by the capacitive process at 60 mV/s. However, due to the incorporation of h-WO$_3$, the percentage contribution from the diffusion-controlled process increases. The P.δ-MnO$_2$/W-b sample shows a maximum diffusion-controlled contribution of 41% at 60 mV/s, verifying the slow reaction kinetics at the low voltage range.

Figure 6b depicts the galvanostatic charge−discharge (GCD) measurements between −0.40 and 0.40 V at 1.5 A

g^{-1} current density to compare the capacitive performance of P.δ-MnO$_2$ and composite materials. From the GCD plot, it is confirmed that all the curves show an asymmetric nonlinear (nonlinear during both the charging and discharging processes) shape with slight distortions due to the pseudocapacitive contribution. This fits with the results of the CV analysis. It was observed that the discharging time of the composite increases compared to P.δ-MnO$_2$, suggesting improvement of the capacitive behavior of P.δ-MnO$_2$ due to the incorporation of h-WO$_3$ nanorods, which might have opened many more pathways and transport channels for the ion's movement and accumulation that are extremely beneficial to the penetration of electrons and the entry of the electrolyte into electrode materials. This special structure of rod-and-sheet-type architecture facilitates the accumulation and diffusion of charges in the interior of the P.δ-MnO$_2$ nanosheets. Additionally, composite electrodes show elongated horizontal discharge curves compared to those of P.δ-MnO$_2$, suggesting a greater amount of Na$^+$ ion insertion into the composite materials. The GCD plots were also used to find the specific capacitances (C_{sp}) using eq 1.

The specific capacitance (Figure 6c) obtained from the GCD curves was 109.8 F g^{-1} for P.δ-MnO$_2$, 154.8 F g^{-1} for P.δ-MnO$_2$/W-a, 363.8 F g^{-1} for P.δ-MnO$_2$/W-b, and 147.4 for P.δ-MnO$_2$/W-c at the 1.5 A g^{-1} current density. The specific capacitance of blank h-WO$_3$ is provided in the Supporting Information. The C_{sp} of P.δ-MnO$_2$ flowers is partly due to their morphology and the intercalated K$^+$ ion. The mesoporous structure with large voids and a large specific surface area of P.δ-MnO$_2$ flowers helps the electrolyte come in contact with P.δ-MnO$_2$ and shorten the path for the deep intercalation and extraction of Na$^+$ ions by providing porous channels to increase the specific capacitance, as discussed before. The increased specific capacitances for the composites ensure that the incorporation of h-WO$_3$ has enhanced the charge storage capacity. The P.δ-MnO$_2$/W-b composite has the longest discharging time and the largest integral area below the GCD curve compared with the other electrode materials, indicating the maximum specific capacitance. This high capacitance behavior of P.δ-MnO$_2$/W-b indicates easy charge migration, providing larger flow paths to enhance the charge storage.

Furthermore, during the initiation of discharge, there was a sharp drop in potential, which indicates energy losses because of the internal resistance.[66] During initial discharge, this sudden drop in potential (*iR* drop) for the P.δ-MnO$_2$/W-b electrode is much smaller (Figure 6b) than the other electrode materials in this study, suggesting higher conductivity and lesser internal resistance of the P.δ-MnO$_2$/W-b electrode, among others. To store energy and keep it from being lost or turned into heat during charging and discharge, the electrode with the lowest internal resistance is very important. At the time of charging and discharging, energy dissipation was eliminated for lower internal resistance material, and energy storage performance improved.[67] So, to fabricate power-saving supercapacitors, a P.δ-MnO$_2$/W-b nanocomposite is more preferable. However, increasing the concentration of h-WO$_3$ can reduce the effective surface area and increase the electrical resistance due to structural deformation. This ultimately leads to poor specific capacitance along with a reduced faradaic redox process in the electrode. This might have been the case for the P.δ-MnO$_2$/W-c composite electrode.

Moreover, the impact of current density on the electrode material's C_{sp} was studied at different current densities of 1.5, 2, and 2.5 A g^{-1} (Figure S4). The existence of a voltage plateau in the discharge curves confirms the pseudocapacitive features of all the electrodes.[68] From Figure S4, it was evident that the charge and discharge periods were shortened by increasing the current density due to the insufficient utilization rate of the electroactive sites. As a result, C_{sp} decreases with increasing current densities. As a result of the high current density, the redox reaction is sluggish, because of the restricted time and contact between the electrolyte and the electrode. As the current density goes up even more, electrolyte ions lose their ability to penetrate and can only be adsorbed to the electrode's upper surface, giving an almost symmetrical triangle-shape GCD curve as noticed for 2.5 A g^{-1} current density (Figure S4). But lower current densities make it easier for electrolyte ions to be adsorbed to the electrode surface and to penetrate the interior of the electrode, giving a high C_{sp}. The variation of specific capacitance with increasing current densities for all of the electrode samples is plotted in Figure 6d.

The electrochemical impedance spectroscopy (EIS) test was performed to investigate the ion diffusion tendency, resistance between the electrode and the electrolyte, and internal resistance of the P.δ-MnO$_2$ and composite electrodes. The EIS technique is useful for probing the underlying mechanism of charge transfer. Figure 6e shows the Nyquist plots of all of the prepared samples. The distinct region provided by the Nyquist plot for the supercapacitor explains charge transfer-limited processes and diffusion-limited processes. Typically, the so-called knee frequency may be used to separate the Nyquist plot into a high-frequency semicircle and a low-frequency inclined line, as illustrated in Figure 6e. In the beginning of the half-circle, there is a nonzero intersection with the real impedance axis. This gives the equivalent series resistance (R_s), which is made up of the bulk resistance of the electrode, the ionic resistance of the electrolyte, and the contact resistance between the active material and the current collector.[69] The charge transfer resistance (R_{ct}) and double layer capacitance at the electrode/electrolyte interface are presented by the semicircle in the high-to-medium frequency range. Notably, the inclined straight line (angled to the Z'-axis of the Nyquist plot) corresponds to the mass transfer resistance (Warburg impedance, Z_w) that is influenced by the diffusion of Na$^+$ on the electrodes' surface.

A modified Randles circuit with resistors and capacitors set up in series and parallel was used to fit the Nyquist plots. Based on the proposed matching circuit exhibited in Figure 6f, the P.δ-MnO$_2$ electrode has the highest value of R_s (3.95 Ω). By going from P.δ-MnO$_2$ > P.δ-MnO$_2$/W-c > P.δ-MnO$_2$/W-a > P.δ-MnO$_2$/W-b, the diameters of semicircles get smaller, showing that R_{ct} is the smallest for the P.δ-MnO$_2$/W-b (4.34 Ω), indicating lower charge-transfer resistance, which would facilitate faster diffusion of the electrons and electrolyte ions. The highest R_{ct} (8.46 Ω) of P.δ-MnO$_2$ could be explained by the lack of h-WO$_3$, which provides high conductivity, increased surface area, and an electron pathway that ultimately improves electron transfer between the layers of the host material. All of the electrodes on the Nyquist plot have slopes between 45° and 90° in the low-frequency range, indicating that the electrodes were operating with both capacitive and diffusion-controlled characteristics. As the P.δ-MnO$_2$/W-b composite electrode exhibited a larger slope than the remaining electrodes, it has superior ion diffusion rate capability. All of

these results indicate that the P.δ-MnO$_2$/W-b composite electrode has a charge-carrying velocity that is faster than others. Therefore, the P.δ-MnO$_2$/W-b composite electrode has a higher C_{sp} than the other electrodes. Due to the large interlayer distance of the P.δ-MnO$_2$/W-b composite, electrolyte gets easy access, and as a result, charge transfer resistance decreases. Also, this reduced diffusive resistance would give better cycling performance to the P.δ-MnO$_2$/W-b composite at the time of the electrochemical stability test. However, both R_{ct} and R_s increased when h-WO$_3$ was loaded at high concentrations to make the composite P.δ-MnO$_2$/W-c, indicating the deterioration of the diffusion characteristics of the electrode materials due to the agglomeration of the layered structure. The results from EIS agree well with those from CV and GCD analyses, clearly showing that the electrodes of nanostructured composite materials have low resistance compared to P.δ-MnO$_2$ for charges to move between the electrolyte and electrode.

Notably, the operational efficiency that determines how well SCs may be used as energy storage devices significantly depends on their energy density, E (W h kg^{-1}) and power density, P (W kg^{-1}), which can be assessed from the GCD curves using eqs 2 and 3. Figure 7a illustrates the Ragone plot
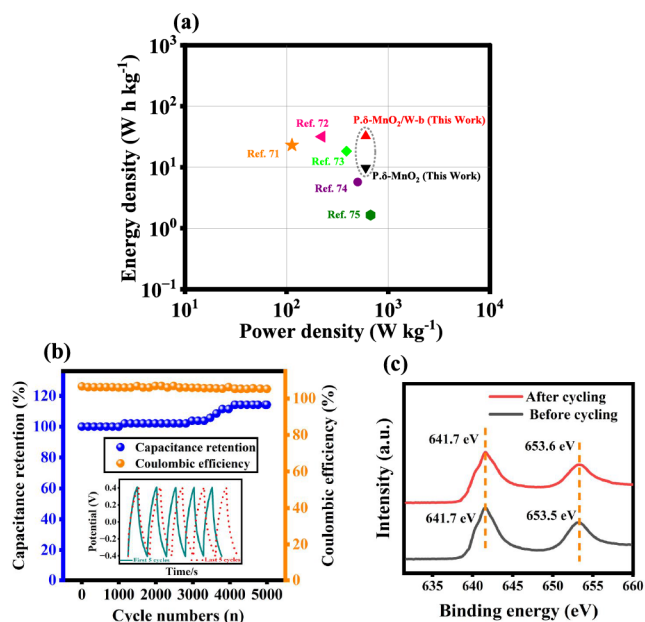
Figure 7. (a) Ragone plot of the synthesized samples. (b) Long-term capacitance retention and columbic efficiency of the P.δ-MnO$_2$/W-b composite electrode over 5000 cycles of operation. (c) Mn 2p core level spectra of the P.δ-MnO$_2$/W-b composite before and after the cycling effect.

(energy density vs power density) for the samples at 1.5 A g^{-1} current density. The values are well in the SC region. We observed that for P.δ-MnO$_2$/W-b composite, the highest energy density is 32.3 W h kg^{-1} at a power density of 600 W kg^{-1}, which is 229.5%, 146.5%, and 134.1% higher than P.δ-MnO$_2$ (9.8 W h kg^{-1}), P.δ-MnO$_2$/W-c (13.1 W h kg^{-1}), and P.δ-MnO$_2$/W-a (13.8 W h kg^{-1}), respectively. Furthermore, this proves that the supportive materials provide synergetic action to improve the electrochemical performance of host P.δ-MnO$_2$ by making it easier for electrons to flow and giving it a large surface area with more redox sites. For comparative

purpose, the data for common supercapacitors are added to the Ragone plot.[70−74]

Long-term cycle stability is another crucial criterion for practical applications of SC-based devices. To check the electrochemical cycling effect via capacitance retention and Coulombic efficiency of the superior P.δ-MnO$_2$/W-b electrode, it was subjected to repeated GCD tests up to 5000 cycles at a current density of 10 A g^{-1} (Figure 7b). The electrode fascinatingly exhibits an increasing trend of capacitance retention, resulting in an ~14% increase in capacitance from its initial specific capacitance after 5000 cycles. This increased capacitance during cycling is guaranteed by the prolonged charge and discharge times of the P.δ-MnO$_2$/W-b electrode (inset of Figure 7b). The first few cycles serve as a self-activation step, causing the electrolytes to entirely soak the surface of the P.δ-MnO$_2$/W-b electrode.[75] As a result, redox reactions will be facilitated over the entire electrode surface, and the electrode will start to gain capacitance, overcoming the internal resistances of the device.[16] The possible cause of this gain in capacitance is the enhanced wettability of the electrode over time.[76,77] In addition to the enhanced wettability, the flowerlike morphology of P.δ-MnO$_2$ with mesoporous characteristics might also contribute to the electro-activation process. As the electrolyte ions are repeatedly inserted and extracted during the cycle test, the nanosheets of the P.δ-MnO$_2$ nanostructure may tend to be vertical toward the electrode surface; hence, the electrode might become more porous.[78] This might shorten the transportation path for the electrolyte ions and enable access to more electrolyte ions for redox reactions at the electrode. Also, interaction with Na$^+$ ions would create many defective or disordered sites to increase the charge storage capacity of the electrode over time by greatly increasing the material's surface area.[79] Along with these, the electro-activation of the P.δ-MnO$_2$/W-b electrode may also be connected to the presence of K$^+$ ions. By immersion of the electrode in the electrolyte solution, some of the K$^+$ ions would be replaced by Na$^+$ ions in the initial cycles. Upon this release of K$^+$ ions, more electroactive sites are freed to intercalate more Na$^+$ ions into the interlayer of the P.δ-MnO$_2$ nanosheets, as shown in Figure 8. Also, Figure 8 illustrates the intercalation of Na$^+$ ions into the voids of h-WO$_3$ nanorods in a Na$_2$SO$_4$ aqueous electrolyte, which contributes to the enhanced pseudocapacitive perform-
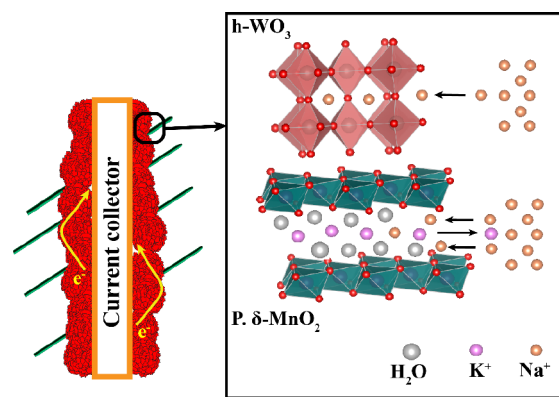
Figure 8. Schematic representation of the Na$^+$ ion intercalation and extraction from the electrolyte into the P.δ-MnO$_2$/W-b composite electrode.

Table 2. Comparison of Electrochemical Performances of P.δ-MnO$_2$/W-b Composites with Already Reported MnO$_2$-based SCs in the Literatures

reported samples	electrolyte	specific capacitance (F g^{-1})	retention rate	references
3D porous birnessite nanosheet	1 M Na$_2$SO$_4$	306 F g^{-1} at 0.2 A g^{-1}	92% (after 1000 cycles)	80
birnessite nanofowers	1 M Na$_2$SO$_4$	197.3 F g^{-1} at 1.0 A g^{-1}	94.6% (after 1000 cycles)	81
CeO@birnessite core−shell heterostructures	1 M KCl	255 F g^{-1} at 0.25 A g^{-1}	90.1% (after 3000 cycles)	82
CoMCNFs@MnO$_2$	1 M Na$_2$SO$_4$	265 F g^{-1} at 0.5 A g^{-1}	98.7% (after 10 000 cycles)	83
MnO$_2$/MXene (nanosheets)	1 M Na$_2$SO$_4$	340 F g^{-1} at 1 A g^{-1}	87.6% (after 2000 cycles)	84
AC/MnO$_2$	1 M Na$_2$SO$_4$	297.8 F g^{-1} at 0.2 A g^{-1}	94.8% (after 1000 cycles)	85
CNFs/MnO$_2$	0.5 M Na$_2$SO$_4$	365 F g^{-1} at 1 A g^{-1}	95.3% (after 1000 cycles)	86
P.δ-MnO$_2$/W-b	0.5 M Na$_2$SO$_4$	363.3 F g^{-1} at 1.5 A g^{-1}	114% (after 5000 cycles)	this work

ance of the P.δ-MnO$_2$/W-b composite electrode compared to the P.δ-MnO$_2$ electrode.

Nyquist plots of the P.δ-MnO$_2$/W-b nanocomposite (the sample with best capacitive performance) were taken after 5000 cycles of operation and presented Figure S7, which demonstrates that the semicircular portion of the impedance spectrum has a lower radius after 5000 cycles. This finding provides additional evidence that this electrode becomes more electrically conductive, has rapid electron-conducting ability at the interface, and reduces its internal resistance after 5000 cycles of operation.[3]

However, the Na$^+$ ion interaction with P.δ-MnO$_2$/W-b can disturb its chemical stability. After a charging−discharging cycle, we analyzed the electrode material by using XPS to identify its chemical states. In agreement with earlier studies, a comparison of the Mn 2p spectra of the P.δ-MnO$_2$/W-b sample before and after 5000 cycles reveals typical peaks of Mn 2p$_{3/2}$ and Mn 2p$_{1/2}$, indicating Mn^{4+} oxidation state in both cases (Figure 7c). Mn 2p spectra show no significant shifts in the oxidation state during long-term cycling, indicating that no chemical changes occurred in the P.δ-MnO$_2$/W-b sample throughout the test. In addition, the Coulombic efficiency was initially found to be ∼106% and remains almost steady up to 5000 cycles, which clearly proves beyond a doubt that no permanent capacity losses have occurred and suggests the superior stability of the P.δ-MnO$_2$/W-b composite. Hence, the P.δ-MnO$_2$/W-b composite electrode in this study has excellent stability along with good specific capacitance and energy density.

Although it is hard to make a precise comparison of all the performance of SCs because of many factors, including charge−discharge rates, material mass loads, and testing setups, one can still make a rough guess, as tabulated in Table 2.

CONCLUSIONS

In summary, we have fabricated a distinctive architecture of advanced three-dimensional binary metal oxide electrodes by growing mesoporous preintercalated δ-MnO$_2$ flowers on h-WO$_3$ nanorods with different weight percentages using a sequential, cost-effective hydrothermal route for high-performance large-scale aqueous supercapacitor. While the XRD studies confirmed the crystallographic structure, the FE-SEM and TEM studies revealed an integration between flowerlike 3D and rodlike 1D morphology in the composites. HR-TEM examination was used to measure the interlayer distance of the prepared electrode materials. The preintercalated cations and water molecules were added to prevent fast oxidation of the δ-MnO$_2$ flowers and provide additional active sites to realize the full usage of δ-MnO$_2$ as an electrode material. Its performance

can be further enhanced by incorporating h-WO$_3$ nanorods. Incorporation of h-WO$_3$ nanorods provided enhanced conductivity, improved redox activity, and more channels for diffusion of electrons and electrolytes to the electrode surface. This investigation opens up the possibility of constructing potential electrodes with not only high specific capacitance and energy density but also excellent cycling stability, an ultrafast charge−discharge rate, excellent durability, and columbic efficiency. In three-electrode configurations, the composites exhibited a specific capacitance of as high as 363.8 F g^{-1}, which is significantly higher than that of the preintercalated δ-MnO$_2$ electrode (109.8 F g^{-1}). The 5 wt % h-WO$_3$ nanorod-incorporated supercapacitor delivered an energy density of 32.3 W h kg^{-1} (at 600 W kg^{-1} power density), and the specific capacitances of the composite have climbed to a higher level upon cycling by enhancing the porosity and active sites, with 114% capacitance retention over 5000 cycles at 10 A g^{-1}. Our study refines old δ-MnO$_2$ into a high-quality electrode material with exceptional electrochemical performance to boost the development of supercapacitors.

■ ASSOCIATED CONTENT

Ⓢ Supporting Information

The Supporting Information is available free of charge at https://pubs.acs.org/doi/10.1021/acsomega.3c09236.

XPS survey spectra of P.δ-MnO$_2$ and P.δ-MnO$_2$/W-b samples (Figure S1); XRD pattern of hexagonal-WO$_3$ (Figure S2); cyclic voltammetry curves of P.δ-MnO$_2$, P.δ-MnO$_2$/W-a, P.δ-MnO$_2$/W-b, and P.δ-MnO$_2$/W-c samples at different scan rates (Figure S3); galvanostatic charging−discharging curves of P.δ-MnO$_2$, P.δ-MnO$_2$/W-a, P.δ-MnO$_2$/W-b, and P.δ-MnO$_2$/W-c samples at different current densities (Figure S4); cyclic voltammetry curves at 60 mV/s, galvanostatic charging−discharging curves at 1.5 A g^{-1} of h-WO$_3$ (Figure S5); the specific capacitance for h-WO$_3$ at 1.5 A g^{-1} current density; decoupling of CV curves of different samples at 60 mV/s scan rate (Figure S6); Nyquist plots of P.δ-MnO$_2$/W-b sample before and after 5000 cycles of charging−discharging (Figure S7) (PDF)

■ AUTHOR INFORMATION

Corresponding Author

Ahmed Sharif − *Department of Materials and Metallurgical Engineering, Bangladesh University of Engineering and Technology, Dhaka 1000, Bangladesh;* ⓞ orcid.org/0000-0002-1592-018X; Email: asharif@mme.buet.ac.bd

Authors

Md Shafayatul Islam − *Department of Materials and Metallurgical Engineering, Bangladesh University of Engineering and Technology, Dhaka 1000, Bangladesh*

Sheikh Manjura Hoque − *Materials Science Division, Atomic Energy Centre, Dhaka 1000, Bangladesh;* ⓘ orcid.org/0000-0002-4233-9374

Mizanur Rahaman − *Department of Physics, Bangladesh University of Engineering and Technology, Dhaka 1000, Bangladesh*

Muhammad Rakibul Islam − *Department of Physics, Bangladesh University of Engineering and Technology, Dhaka 1000, Bangladesh*

Ahmad Irfan − *Department of Chemistry, College of Science, King Khalid University, Abha 61413, Saudi Arabia*

Complete contact information is available at:
https://pubs.acs.org/10.1021/acsomega.3c09236

Author Contributions

The manuscript was written through the contributions of all authors. All authors have given approval to the final version of the manuscript. Md S.I. contributed to conceptualization, methodology, investigation, formal analysis, and writing—original draft. S.M.H. contributed to methodology, formal analysis, and writing—review and editing. M.R. contributed to investigation and formal analysis. M.R.I. contributed to investigation and formal analysis. A.I. contributed to formal analysis and writing—review and editing. A.S. contributed to conceptualization, resources allocation, supervision, and writing—review and editing.

Notes

The authors declare no competing financial interest.

■ REFERENCES

(1) González, A.; Goikolea, E.; Barrena, J. A.; Mysyk, R. Review on Supercapacitors: Technologies and Materials. *Renewable Sustainable Energy Rev.* **2016**, *58*, 1189−1206.

(2) Luo, B.; Ye, D.; Wang, L. Recent Progress on Integrated Energy Conversion and Storage Systems. *Adv. Sci.* **2017**, *4* (9), 1700104.

(3) Mahmood, M.; Rasheed, A.; Ayman, I.; Rasheed, T.; Munir, S.; Ajmal, S.; Agboola, P. O.; Warsi, M. F.; Shahid, M. Synthesis of Ultrathin MnO₂ Nanowire-Intercalated 2D-MXenes for High-Performance Hybrid Supercapacitors. *Energy Fuels* **2021**, *35* (4), 3469−3478.

(4) Xiao, Z.; Mei, Y.; Yuan, S.; Mei, H.; Xu, B.; Bao, Y.; Fan, L.; Kang, W.; Dai, F.; Wang, R.; Wang, L.; Hu, S.; Sun, D.; Zhou, H.-C. Controlled Hydrolysis of Metal−Organic Frameworks: Hierarchical Ni/Co-Layered Double Hydroxide Microspheres for High-Performance Supercapacitors. *ACS Nano* **2019**, *13* (6), 7024−7030.

(5) Bongu, C. S.; Krishnan, M. R.; Soliman, A.; Arsalan, M.; Alsharaeh, E. H. Flexible and Freestanding MoS₂ /Graphene Composite for High-Performance Supercapacitors. *ACS Omega* **2023**, *8* (40), 36789−36800.

(6) Liu, J.; Bao, J.; Zhang, X.; Gao, Y.; Zhang, Y.; Liu, L.; Cao, Z. MnO₂ -Based Materials for Supercapacitor Electrodes: Challenges, Strategies and Prospects. *RSC Adv.* **2022**, *12* (55), 35556−35578.

(7) Qin, H.; Liang, S.; Chen, L.; Li, Y.; Luo, Z.; Chen, S. Recent Advances in Vanadium-Based Nanomaterials and Their Composites for Supercapacitors. *Sustainable Energy Fuels* **2020**, *4* (10), 4902−4933.

(8) Chettiannan, B.; Srinivasan, A. K.; Arumugam, G.; Shajahan, S.; Haija, M. A.; Rajendran, R. Incorporation of α-MnO₂ Nanoflowers into Zinc-Terephthalate Metal−Organic Frameworks for High-Performance Asymmetric Supercapacitors. *ACS Omega* **2023**, *8* (7), 6982−6993.

(9) Devaraj, S.; Munichandraiah, N. Effect of Crystallographic Structure of MnO₂ on Its Electrochemical Capacitance Properties. *J. Phys. Chem. C* **2008**, *112* (11), 4406−4417.

(10) Dixini, P. V. M.; Carvalho, B. B.; Gonçalves, G. R.; Pegoretti, V. C. B.; Freitas, M. B. J. G. Sol−Gel Synthesis of Manganese Oxide Supercapacitor from Manganese Recycled from Spent Zn−MnO2 Batteries Using Organic Acid as a Leaching Agent. *Ionics* **2019**, *25* (9), 4381−4392.

(11) Brousse, T.; Toupin, M.; Dugas, R.; Athouël, L.; Crosnier, O.; Bélanger, D. Crystalline MnO[Sub 2] as Possible Alternatives to Amorphous Compounds in Electrochemical Supercapacitors. *J. Electrochem. Soc.* **2006**, *153* (12), A2171.

(12) Hong, S.; Jin, S.; Deng, Y.; Garcia-Mendez, R.; Kim, K.; Utomo, N.; Archer, L. A. Efficient Scalable Hydrothermal Synthesis of MnO₂ with Controlled Polymorphs and Morphologies for Enhanced Battery Cathodes. *ACS Energy Lett.* **2023**, *8* (4), 1744−1751.

(13) Munaiah, Y.; Sundara Raj, B. G.; Prem Kumar, T.; Ragupathy, P. Facile Synthesis of Hollow Sphere Amorphous MnO2: The Formation Mechanism, Morphology and Effect of a Bivalent Cation-Containing Electrolyte on Its Supercapacitive Behavior. *J. Mater. Chem. A* **2013**, *1* (13), 4300.

(14) Hu, J.; Shen, Y.; Xu, L.; Huang, H. Synthesis of Urchin-like MnO₂ /Reduced Graphene Oxide (RGO) Composite and Their Wave-Absorbing Property. *Mater. Res. Express* **2019**, *6* (9), 095002.

(15) Truong, T. T.; Liu, Y.; Ren, Y.; Trahey, L.; Sun, Y. Morphological and Crystalline Evolution of Nanostructured MnO₂ and Its Application in Lithium−Air Batteries. *ACS Nano* **2012**, *6* (9), 8067−8077.

(16) Sahoo, D.; Shakya, J.; Choudhury, S.; Roy, S. S.; Devi, L.; Singh, B.; Ghosh, S.; Kaviraj, B. High-Performance MnO₂ Nanowire/MoS₂ Nanosheet Composite for a Symmetrical Solid-State Supercapacitor. *ACS Omega* **2022**, *7* (20), 16895−16905.

(17) Alfaruqi, M. H.; Gim, J.; Kim, S.; Song, J.; Pham, D. T.; Jo, J.; Xiu, Z.; Mathew, V.; Kim, J. A Layered δ-MnO2 Nanoflake Cathode with High Zinc-Storage Capacities for Eco-Friendly Battery Applications. *Electrochem. Commun.* **2015**, *60*, 121−125.

(18) Gu, Y.; Xu, D.; Chen, S.; You, F.; Hu, C.; Huang, H.; Chen, J. In Situ Growth of MnO₂ Nanosheets on a Graphite Flake as an Effective Binder-Free Electrode for High-Performance Supercapacitors. *ACS Omega* **2022**, *7* (51), 48320−48331.

(19) Sun, P.; Yi, H.; Peng, T.; Jing, Y.; Wang, R.; Wang, H.; Wang, X. Ultrathin MnO2 Nanoflakes Deposited on Carbon Nanotube Networks for Symmetrical Supercapacitors with Enhanced Performance. *J. Power Sources* **2017**, *341*, 27−35.

(20) Alfaruqi, M. H.; Islam, S.; Putro, D. Y.; Mathew, V.; Kim, S.; Jo, J.; Kim, S.; Sun, Y.-K.; Kim, K.; Kim, J. Structural Transformation and Electrochemical Study of Layered MnO2 in Rechargeable Aqueous Zinc-Ion Battery. *Electrochim. Acta* **2018**, *276*, 1−11.

(21) Pan, H.; Shao, Y.; Yan, P.; Cheng, Y.; Han, K. S.; Nie, Z.; Wang, C.; Yang, J.; Li, X.; Bhattacharya, P.; Mueller, K. T.; Liu, J. Reversible Aqueous Zinc/Manganese Oxide Energy Storage from Conversion Reactions. *Nat. Energy* **2016**, *1* (5), 16039.

(22) Han, G.; Liu, Y.; Zhang, L.; Kan, E.; Zhang, S.; Tang, J.; Tang, W. MnO2 Nanorods Intercalating Graphene Oxide/Polyaniline

Ternary Composites for Robust High-Performance Supercapacitors. *Sci. Rep.* **2014**, *4* (1), 4824.

(23) Patil, S. H.; Gaikwad, A. P.; Waghmode, B. J.; Sathaye, S. D.; Patil, K. R. A Graphene–MnO$_2$ Composite Supercapacitor Material Accomplished Tactically Using Liquid–Liquid and Solid–Liquid Interface Reaction Techniques. *New. J. Chem.* **2020**, *44* (17), 6853–6861.

(24) Yao, C.; Wei, B.; Li, H.; Wang, G.; Han, Q.; Ma, H.; Gong, Q. Carbon-Encapsulated Tungsten Oxide Nanowires as a Stable and High-Rate Anode Material for Flexible Asymmetric Supercapacitors. *J. Mater. Chem. A* **2017**, *5* (1), 56–61.

(25) Yuan, C.; Li, M.; Wang, M. Formation Mechanism of WO2(OH)2-MnO2 Composite via Electro-Codeposition and Electrochemical Origin of Its Improved Supercapacitive Performance. *Electrochim. Acta* **2017**, *245*, 463–471.

(26) Lokhande, V.; Lokhande, A.; Namkoong, G.; Kim, J. H.; Ji, T. Charge Storage in WO3 Polymorphs and Their Application as Supercapacitor Electrode Material. *Results Phys.* **2019**, *12*, 2012–2020.

(27) Wang, D.; Wang, L.; Liang, G.; Li, H.; Liu, Z.; Tang, Z.; Liang, J.; Zhi, C. A Superior δ-MnO$_2$ Cathode and a Self-Healing Zn-δ-MnO$_2$ Battery. *ACS Nano* **2019**, *13* (9), 10643–10652.

(28) Xiong, T.; Lee, W. S. V.; Xue, J. K$^+$-Intercalated MnO$_2$ Electrode for High Performance Aqueous Supercapacitor. *ACS Appl. Energy Mater.* **2018**, *1*, 5619–5626.

(29) Meng, Y.; Song, W.; Huang, H.; Ren, Z.; Chen, S.-Y.; Suib, S. L. Structure–Property Relationship of Bifunctional MnO$_2$ Nanostructures: Highly Efficient, Ultra-Stable Electrochemical Water Oxidation and Oxygen Reduction Reaction Catalysts Identified in Alkaline Media. *J. Am. Chem. Soc.* **2014**, *136* (32), 11452–11464.

(30) Justin Raj, C.; Manikandan, R.; Sivakumar, P.; Opar, D. O.; Dennyson Savariraj, A.; Cho, W.-J.; Jung, H.; Kim, B. C. Origin of Capacitance Decay for a Flower-like δ-MnO2 Aqueous Supercapacitor Electrode: The Quantitative Surface and Electrochemical Analysis. *J. Alloys Compd.* **2022**, *892*, 162199.

(31) Rivera-Lugo, Y. Y.; Félix-Navarro, R. M.; Trujillo-Navarrete, B.; Reynoso-Soto, E. A.; Silva-Carrillo, C.; Cruz-Gutiérrez, C. A.; Quiroga-González, E.; Calva-Yáñez, J. C. Flower-like δ-MnO2 as Cathode Material of Li-Ion Batteries of High Charge-Discharge Rates. *Fuel* **2021**, *287*, 119463.

(32) Park, B.-H.; Choi, J.-H. Improvement in the Capacitance of a Carbon Electrode Prepared Using Water-Soluble Polymer Binder for a Capacitive Deionization Application. *Electrochim. Acta* **2010**, *55* (8), 2888–2893.

(33) Tarek, Y. A.; Shakil, R.; Reaz, A. H.; Roy, C. K.; Barai, H. R.; Firoz, S. H. Wrinkled Flower-Like rGO Intercalated with Ni(OH)$_2$ and MnO$_2$ as High-Performing Supercapacitor Electrode. *ACS Omega* **2022**, *7* (23), 20145–20154.

(34) Oyedotun, K. O.; Mirghni, A. A.; Fasakin, O.; Tarimo, D. J.; Mahmoud, B. A.; Manyala, N. Effect of Growth-Time on Electrochemical Performance of Birnessite Manganese Oxide (δ-MnO2) as Electrodes for Supercapacitors: An Insight into Neutral Aqueous Electrolytes. *J. Energy Storage* **2021**, *36*, 102419.

(35) Din Sheikh, M. U.; Naikoo, G. A.; Thomas, M.; Bano, M.; Ahirwar, D.; Pandit, U. J.; Khan, F. Fabrication of Hierarchically Mesoporous CuO Nanostructures and Their Role as Heterogenous Catalysts and Sensors. *RSC Adv.* **2016**, *6* (49), 42807–42818.

(36) Cremonezzi, J. M. D. O.; Tiba, D. Y.; Domingues, S. H. Fast Synthesis of δ-MnO2 for a High-Performance Supercapacitor Electrode. *Sn. Appl. Sci.* **2020**, *2* (10), 1689.

(37) Ladd, M. F. C.; Palmer, R. A.; Palmer, R. A. *Structure Determination by X-Ray Crystallography*; Springer, 1977; Vol. *233*.

(38) Ghodbane, O.; Pascal, J.-L.; Favier, F. Microstructural Effects on Charge-Storage Properties in MnO$_2$-Based Electrochemical Supercapacitors. *ACS Appl. Mater. Interfaces* **2009**, *1* (5), 1130–1139.

(39) Chen, W.; Li, G.; Pei, A.; Li, Y.; Liao, L.; Wang, H.; Wan, J.; Liang, Z.; Chen, G.; Zhang, H.; Wang, J.; Cui, Y. A Manganese–Hydrogen Battery with Potential for Grid-Scale Energy Storage. *Nat. Energy* **2018**, *3* (5), 428–435.

(40) Jain, S.; Shah, J.; Negi, N. S.; Sharma, C.; Kotnala, R. K. Significance of Interface Barrier at Electrode of Hematite Hydroelectric Cell for Generating Ecopower by Water Splitting. *Int. J. Energy Res.* **2019**, *43* (9), 4743–4755.

(41) Yuan, A.; Wang, X.; Wang, Y.; Hu, J. Textural and Capacitive Characteristics of MnO2 Nanocrystals Derived from a Novel Solid-Reaction Route. *Electrochim. Acta* **2009**, *54* (3), 1021–1026.

(42) Kitchaev, D. A.; Dacek, S. T.; Sun, W.; Ceder, G. Thermodynamics of Phase Selection in MnO$_2$ Framework Structures through Alkali Intercalation and Hydration. *J. Am. Chem. Soc.* **2017**, *139* (7), 2672–2681.

(43) Wei, D.; Ding, Y.; Li, Z. Noble-Metal-Free Z-Scheme MoS2–CdS/WO3–MnO2 Nanocomposites for Photocatalytic Overall Water Splitting under Visible Light. *Int. J. Hydrogen. Energy* **2020**, *45* (35), 17320–17328.

(44) Kalanur, S. S. Structural Optical, Band Edge and Enhanced Photoelectrochemical Water Splitting Properties of Tin-Doped WO3. *Catalysts* **2019**, *9* (5), 456.

(45) Srinivasulu, T.; Saritha, K.; Reddy, K. T. R. Synthesis and Characterization of Fe-Doped ZnO Thin Films Deposited by Chemical Spray Pyrolysis. *Mod. Electron. Mater.* **2017**, *3* (2), 76–85.

(46) Singh, S. J.; Lim, Y. Y.; Hmar, J. J. L.; Chinnamuthu, P. Temperature Dependency on Ce-Doped CuO Nanoparticles: A Comparative Study via XRD Line Broadening Analysis. *Appl. Phys. A Mater. Sci. Process* **2022**, *128* (3), 188.

(47) Gigot, A.; Fontana, M.; Serrapede, M.; Castellino, M.; Bianco, S.; Armandi, M.; Bonelli, B.; Pirri, C. F.; Tresso, E.; Rivolo, P. Mixed 1T–2H Phase MoS$_2$/Reduced Graphene Oxide as Active Electrode for Enhanced Supercapacitive Performance. *ACS Appl. Mater. Interfaces* **2016**, *8* (48), 32842–32852.

(48) Robert, R.; Novák, P. Structural Changes and Microstrain Generated on LiNi$_{0.80}$Co$_{0.15}$Al$_{0.05}$O$_2$ during Cycling: Effects on the Electrochemical Performance. *J. Electrochem. Soc.* **2015**, *162* (9), A1823–A1828.

(49) Su, R.; Wang, H.; Sun, Y.; Guo, P. Structural Regulation of Porous MnO2 Nanosheets and Their Electrocapacitive Behavior in Aqueous Electrolytes. *Colloids Surf. A* **2021**, *609*, 125579.

(50) Li, J.; Huang, J.; Li, J.; Cao, L.; Qi, H.; Cheng, Y.; Xi, Q.; Dang, H. Improved Li-Ion Diffusion Process in TiO2/rGO Anode for Lithium-Ion Battery. *J. Alloys Compd.* **2017**, *727*, 998–1005.

(51) Shinde, P. A.; Lokhande, A. C.; Chodankar, N. R.; Patil, A. M.; Kim, J. H.; Lokhande, C. D. Temperature Dependent Surface Morphological Modifications of Hexagonal WO3 Thin Films for High Performance Supercapacitor Application. *Electrochim. Acta* **2017**, *224*, 397–404.

(52) Sha, R.; Gopalakrishnan, A.; Sreenivasulu, K. V.; Srikanth, V.; S, V. S.; Badhulika, S. Template-Cum-Catalysis Free Synthesis of α-MnO2 Nanorods-Hierarchical MoS2Microspheres Composite for Ultra-Sensitive and Selective Determination of Nitrite. *J. Alloys Compd.* **2019**, *794*, 26–34.

(53) Duan, X.; Xiao, S.; Wang, L.; Huang, H.; Liu, Y.; Li, Q.; Wang, T. Ionic Liquid-Modulated Preparation of Hexagonal Tungsten Trioxide Mesocrystals for Lithium-Ion Batteries. *Nanoscale* **2015**, *7* (6), 2230–2234.

(54) Hu, L.; Ren, Y.; Yang, H.; Xu, Q. Fabrication of 3D Hierarchical MoS$_2$/Polyaniline and MoS$_2$/C Architectures for Lithium-Ion Battery Applications. *ACS Appl. Mater. Interfaces* **2014**, *6* (16), 14644–14652.

(55) Xiao, B. Intercalated Water in Aqueous Batteries. *Carbon Energy* **2020**, *2* (2), 251–264.

(56) Wu, Z.; Tang, C.; Zhou, P.; Liu, Z.; Xu, Y.; Wang, D.; Fang, B. Enhanced Hydrogen Evolution Catalysis from Osmotically Swollen Ammoniated MoS$_2$. *J. Mater. Chem. A* **2015**, *3* (24), 13050–13056.

(57) Sharma, M.; Sundriyal, S.; Panwar, A.; Gaur, A. Enhanced Supercapacitive Performance of Ni0.5Mg0.5Co2O4 Flowers and Rods as an Electrode Material for High Energy Density Supercapacitors: Rod Morphology Holds the Key. *J. Alloys Compd.* **2018**, *766*, 859–867.

(58) Wu, Q.; He, T.; Zhang, Y.; Zhang, J.; Wang, Z.; Liu, Y.; Zhao, L.; Wu, Y.; Ran, F. Cyclic Stability of Supercapacitors: Materials, Energy Storage Mechanism, Test Methods, and Device. *J. Mater. Chem. A* **2021**, *9* (43), 24094–24147.

(59) Ali, B. A.; Metwalli, O. I.; Khalil, A. S. G.; Allam, N. K. Unveiling the Effect of the Structure of Carbon Material on the Charge Storage Mechanism in MoS$_2$ -Based Supercapacitors. *ACS Omega* **2018**, *3* (11), 16301–16308.

(60) Kuo, S.-L.; Lee, J.-F.; Wu, N.-L. Study on Pseudocapacitance Mechanism of Aqueous MnFe[Sub 2]O[Sub 4] Supercapacitor. *J. Electrochem. Soc.* **2007**, *154* (1), A34.

(61) Ghosh, S. K. Diversity in the Family of Manganese Oxides at the Nanoscale: From Fundamentals to Applications. *ACS Omega* **2020**, *5* (40), 25493–25504.

(62) Mulik, S. V.; Dhas, S. D.; Moholkar, A. V.; Parale, V. G.; Park, H.-H.; Koyale, P. A.; Ghodake, V. S.; Panda, D. K.; Delekar, S. D. Square-Facet Nanobar MOF-Derived Co$_3$O$_4$@Co/N-Doped CNT Core–Shell-Based Nanocomposites as Cathode Materials for High-Performance Supercapacitor Studies. *ACS Omega* **2023**, *8* (2), 2183–2196.

(63) Hao, S.; Ji, X.; Liu, F.; Zhong, S.; Pang, K. Y.; Lim, K. G.; Chong, T. C.; Zhao, R. Monolayer MoS$_2$/WO$_3$ Heterostructures with Sulfur Anion Reservoirs as Electronic Synapses for Neuromorphic Computing. *ACS Appl. Nano Mater.* **2021**, *4* (2), 1766–1775.

(64) Ramalingam, R. J.; Konikkara, N.; Al-Lohedan, H.; Al-Dhayan, D. M.; Kennedy, L. J.; Basha, S. K. K.; Sayed, S. R. M. Synthesis of MoS2 Nanoparticle Deposited Graphene/Mesoporous MnOx Nanocomposite for High Performance Super Capacitor Application. *Int. J. Hydrogen. Energy* **2018**, *43* (36), 17121–17131.

(65) Zhi, J.; Reiser, O.; Huang, F. Hierarchical MnO$_2$ Spheres Decorated by Carbon-Coated Cobalt Nanobeads: Low-Cost and High-Performance Electrode Materials for Supercapacitors. *ACS Appl. Mater. Interfaces* **2016**, *8* (13), 8452–8459.

(66) Bhujun, B.; Tan, M. T. T.; Shanmugam, A. S. Study of Mixed Ternary Transition Metal Ferrites as Potential Electrodes for Supercapacitor Applications. *Results Phys.* **2017**, *7*, 345–353.

(67) Xie, Y.; Du, H. Electrochemical Capacitance of a Carbon Quantum Dots–Polypyrrole/Titania Nanotube Hybrid. *RSC Adv.* **2015**, *5* (109), 89689–89697.

(68) Hu, L.; Chen, W.; Xie, X.; Liu, N.; Yang, Y.; Wu, H.; Yao, Y.; Pasta, M.; Alshareef, H. N.; Cui, Y. Symmetrical MnO$_2$ – Carbon Nanotube–Textile Nanostructures for Wearable Pseudocapacitors with High Mass Loading. *ACS Nano* **2011**, *5* (11), 8904–8913.

(69) Gaire, M.; Liang, K.; Luo, S.; Subedi, B.; Adireddy, S.; Schroder, K.; Farnsworth, S.; Chrisey, D. B. Nanostructured Manganese Oxides Electrode with Ultra-Long Lifetime for Electrochemical Capacitors. *RSC Adv.* **2020**, *10* (28), 16817–16825.

(70) Reaz, A. H.; Saha, S.; Roy, C. K.; Wahab, M. A.; Will, G.; Amin, M. A.; Yamauchi, Y.; Liu, S.; Kaneti, Y. V.; Hossain, M. S.; Firoz, S. H. Boosting Capacitive Performance of Manganese Oxide Nanorods by Decorating with Three-Dimensional Crushed Graphene. *Nano Convergence* **2022**, *9* (1), 10.

(71) Liu, Y.; Miao, X.; Fang, J.; Zhang, X.; Chen, S.; Li, W.; Feng, W.; Chen, Y.; Wang, W.; Zhang, Y. Layered-MnO$_2$ Nanosheet Grown on Nitrogen-Doped Graphene Template as a Composite Cathode for Flexible Solid-State Asymmetric Supercapacitor. *ACS Appl. Mater. Interfaces* **2016**, *8* (8), 5251–5260.

(72) Ghosh, K.; Yue, C. Y.; Sk, M. M.; Jena, R. K.; Bi, S. Development of a 3D Graphene Aerogel and 3D Porous Graphene/MnO$_2$@polyaniline Hybrid Film for All-Solid-State Flexible Asymmetric Supercapacitors. *Sustainable Energy Fuels* **2018**, *2* (1), 280–293.

(73) Luan, Z.; Tian, Y.; Gai, L.; Jiang, H.; Guo, X.; Yang, Y. Environment-Benign Synthesis of rGO/MnO Nanocomposites with Superior Electrochemical Performance for Supercapacitors. *J. Alloys Compd.* **2017**, *729*, 9–18.

(74) Wang, S.; Pei, B.; Zhao, X.; Dryfe, R. A. W. Highly Porous Graphene on Carbon Cloth as Advanced Electrodes for Flexible All-Solid-State Supercapacitors. *Nano Energy* **2013**, *2* (4), 530–536.

(75) Qu, Q.; Zhang, P.; Wang, B.; Chen, Y.; Tian, S.; Wu, Y.; Holze, R. Electrochemical Performance of MnO$_2$ Nanorods in Neutral Aqueous Electrolytes as a Cathode for Asymmetric Supercapacitors. *J. Phys. Chem. C* **2009**, *113* (31), 14020–14027.

(76) Ling, Z.; Wang, Z.; Zhang, M.; Yu, C.; Wang, G.; Dong, Y.; Liu, S.; Wang, Y.; Qiu, J. Sustainable Synthesis and Assembly of Biomass-Derived B/N Co-Doped Carbon Nanosheets with Ultrahigh Aspect Ratio for High-Performance Supercapacitors. *Adv. Funct. Mater.* **2016**, *26* (1), 111–119.

(77) Xu, K.; Li, S.; Yang, J.; Xu, H.; Hu, J. Hierarchical MnO2 Nanosheets on Electrospun NiCo2O4 Nanotubes as Electrode Materials for High Rate Capability and Excellent Cycling Stability Supercapacitors. *J. Alloys Compd.* **2016**, *678*, 120–125.

(78) Shao, J.; Zhou, X.; Liu, Q.; Zou, R.; Li, W.; Yang, J.; Hu, J. Mechanism Analysis of the Capacitance Contributions and Ultralong Cycling-Stability of the Isomorphous MnO$_2$@MnO$_2$ Core/Shell Nanostructures for Supercapacitors. *J. Mater. Chem. A* **2015**, *3* (11), 6168–6176.

(79) Chen, W.; Rakhi, R. B.; Wang, Q.; Hedhili, M. N.; Alshareef, H. N. Morphological and Electrochemical Cycling Effects in MnO$_2$ Nanostructures by 3D Electron Tomography. *Adv. Funct. Mater.* **2014**, *24* (21), 3130–3143.

(80) Gao, P.; Metz, P.; Hey, T.; Gong, Y.; Liu, D.; Edwards, D. D.; Howe, J. Y.; Huang, R.; Misture, S. T. The Critical Role of Point Defects in Improving the Specific Capacitance of δ-MnO2 Nanosheets. *Nat. Commun.* **2017**, *8* (1), 14559.

(81) Zhao, S.; Liu, T.; Hou, D.; Zeng, W.; Miao, B.; Hussain, S.; Peng, X.; Javed, M. S. Controlled Synthesis of Hierarchical Birnessite-Type MnO$_2$ Nanoflowers for Supercapacitor Applications. *Appl. Surf. Sci.* **2015**, *356*, 259–265.

(82) Zhu, S. J.; Jia, J. Q.; Wang, T.; Zhao, D.; Yang, J.; Dong, F.; Shang, Z. G.; Zhang, Y. X. Rational Design of Octahedron and Nanowire CeO$_2$@MnO$_2$ Core–Shell Heterostructures with Outstanding Rate Capability for Asymmetric Supercapacitors. *Chem. Commun.* **2015**, *51* (80), 14840–14843.

(83) Sun, X.; Xu, T.; Bai, J.; Li, C. MnO$_2$ Nanosheets Grown on Multichannel Carbon Nanofibers Containing Amorphous Cobalt Oxide as a Flexible Electrode for Supercapacitors. *ACS Appl. Energy Mater.* **2019**, *2* (12), 8675–8684.

(84) Chen, S.; Xiang, Y.; Xu, W.; Peng, C. A Novel MnO$_2$/MXene Composite Prepared by Electrostatic Self-Assembly and Its Use as an Electrode for Enhanced Supercapacitive Performance. *Inorg. Chem. Front.* **2019**, *6* (1), 199–208.

(85) Kim, S.; Lee, J.; Kang, J. S.; Jo, K.; Kim, S.; Sung, Y.-E.; Yoon, J. Lithium Recovery from Brine Using a λ-MnO2/Activated Carbon Hybrid Supercapacitor System. *Chemosphere* **2015**, *125*, 50–56.

(86) Wang, J.-G.; Yang, Y.; Huang, Z.-H.; Kang, F. Effect of Temperature on the Pseudo-Capacitive Behavior of Freestanding MnO2@carbon Nanofibers Composites Electrodes in Mild Electrolyte. *J. Power Sources* **2013**, *224*, 86–92.